Structure Low Dimensionality and Lone-Pair Stereochemical Activity: the Key to Low Thermal Conductivity in the Pb–Sn–S System

Paribesh Acharyya, Koushik Pal, Bin Zhang, Tristan Barbier, Carmelo Prestipino, Philippe Boullay, Bernard Raveau, P. Lemoine, Bernard Malaman, Xingchen Shen, et al.

Structure low dimensionality and lone pair stereochemical activity, the key to low thermal conductivity in Pb-Sn-S system

Paribesh Acharyya,[1,*] Koushik Pal,[2,3] Bin Zhang,[4,5,*] Tristan Barbier,[1] Carmelo Prestipino,[1] Philippe Boullay,[1] Bernard Raveau,[1] Pierric Lemoine,[6] Bernard Malaman,[6] Xingchen Shen,[1] Maxime Vaillant,[1]Adèle Renaud,[7] Blas P. Uberuaga,[3] Christophe Candolfi,[6] Xiaoyuan Zhou,[4,5] Emmanuel Guilmeau[1,*]

[1]*CRISMAT, CNRS, Normandie Univ, ENSICAEN, UNICAEN, 14000 Caen, France*

[2]*Dept. of Physics, IIT Kanpur, Kanpur 208016, India*

[3]*Materials Science and Technology Division, Los Alamos National Laboratory, Los Alamos 87545, USA*

[4]*College of Physics and Institute of Advanced Interdisciplinary Studies, Chongqing University, Chongqing 401331, China*

[5]*Analytical and Testing Center of Chongqing University, Chongqing 401331, China*

[6] *Institut Jean Lamour, UMR 7198 CNRS – Université de Lorraine, 54011 Nancy, France*

[7]*Univ Rennes, ISCR – UMR 6226, CNRS, F-35000 Rennes, France*

**Corresponding authors: paribesh.acharyya@ensicaen.fr; welon5337@126.com; emmanuel.guilmeau@ensicaen.fr;*

Abstract

Recently, metal sulphides have begun to receive attention as potential cost-effective materials for thermoelectric applications beyond optoelectronic and photovoltaic devices. Herein, based on a comparative analysis of the structural and transport properties of 2D-$PbSnS_2$ and 1D-$PbSnS_3$, we demonstrate that the intrinsic effects that govern the low lattice thermal conductivity (κ_L) of these sulfides originate from the combination of the low dimensionality of their crystal structures with the stereochemical activity of the lone pair electrons of cations. The presence of weak bonds in these materials, responsible for phonon scattering, results in inherently low κ_L of 1.0 W/m.K in 1D-$PbSnS_3$ and 0.6 W/m.K in 2D-$PbSnS_2$ at room temperature. However, the nature of the thermal transport is quite distinct. 1D-$PbSnS_3$ exhibits a higher thermal conductivity with a crystalline-like peak at low temperatures, while 2D-$PbSnS_2$ demonstrates glassy thermal conductivity in the entire temperature range investigated. First principles density functional theory calculations reveal that the presence of antibonding states below the Fermi level, especially in $PbSnS_2$, contributes to the very low κ_L. In addition, the calculated phonon dispersions exhibit very soft acoustic phonon branches that give rise to soft lattice and very low speed of sounds.

Introduction

Heat propagates through a solid via electrons and lattice vibrations (phonons).[1, 2] For a crystalline electrical insulator, phonons are the primary carrier of thermal energy, as the electronic contribution (κ_{ele}) to the total thermal conductivity (κ) is negligible.[3] The fundamental understanding of thermal transport through a crystalline material is a long-lasting challenge due to many body interactions at the structural and microscopic levels.[1] Therefore, analysing the lattice thermal conductivity, κ_L from a crystal structure and chemical bonding viewpoint has gained widespread attention.[4, 5] Materials with high lattice thermal conductivity are investigated for heat dissipation in electronics and thermal energy transmission,[6, 7] while low thermal conductive materials are studied for thermal barrier coating,[8] hot phonon bottleneck in photovoltaics[9] and thermoelectrics.[10, 11] Low κ_L depends on the strength of phonon scattering, which can be enhanced through different approaches/phenomena, such as nano/meso structuring,[12] loosely bounded atoms in open crystal structures referred to as rattling,[13] point defects,[14] or lattice anharmonicity,[5, 15] etc. Most of these strategies have been mainly investigated in skutterudites, clathrates, heavy metal selenides and tellurides.[3, 5, 16, 17]

Metal sulphides usually present higher lattice thermal conductivity compared to selenides and tellurides, due to the light atomic weight of sulphur.[18] However, they are inexpensive and earth-abundant, providing price stability and long-term availability.[19] Thus, significant attention is given to the development of sulphide-based materials with ultralow lattice thermal conductivity for thermoelectric applications.[20] To achieve intrinsically low κ_L, sulphides should possess a complex crystal structure associated to order/disorder phenomena as in colusites $Cu_{26}T_2Sn_6S_{32}$ (T = V, Nb, Ta),[21-23] mobiles ions in a superionic lattice ($Cu_{2-x}S$),[24, 25] lone pair induced high anharmonicity ($AgBiS_2$, $CuBiS_2$, $Cu_{12}Sb_4S_{13}$, $Cu_{1-x}\square_xPb_{1-x}Bi_{1+x}S_3$, bournonite $PbCuSbS_3$),[26-32] intrinsic rattlers ($Cu_{12}Sb_4S_{13}$, $AgBi_3S_5$, $Cu_{1.6}Bi_{4.8}S_8$),[32-36] or two-dimensional layered crystal structure (SnS).[19, 37, 38] Recently, S. Zhan *et al.*[39] have achieved a maximum ZT of ~1.2 at 773 K and an average ZT of ~0.75 in the temperature range of 300-773 K in Cl-doped $PbSnS_2$ (isostructural to SnS) combining optimized carrier concentration (*n*-type) and intrinsically low κ_L of 0.6 W/m.K at 300 K.

However, the transport properties of bulk polycrystalline samples of $PbSnS_2$ remain so far unknown and a detailed understanding of the origin of their very low κ_L is yet to be fully achieved, which is fundamental to design bulk efficient materials with low lattice thermal conductivity for various possible applications, as discussed earlier. With this motivation, we have synthesised bulk polycrystalline $PbSnS_2$ sample via mechanical alloying and spark plasma

sintering and compared its thermal transport and vibrational properties with a sample of $PbSnS_3$. Using a combination of experimental results and theoretical calculations, we show that the origin of the low κ_L values in both compounds is tied to the low dimensionalities of the structures in relation to the stereochemical activity of Pb^{2+} and Sn^{2+} lone pairs in 2D $PbSnS_2$, and only Pb^{2+} lone pair in 1D $PbSnS_3$. These results enrich the fundamental knowledges of crystal chemistry and thermal conduction relationships in metal sulphides.

Results and Discussion

Crystal structures

$PbSnS_3$, known as suredaite mineral,[40] has a one-dimensional orthorhombic crystal structure (space group *Pnma*, No 62)[41] which consists of double columns of edge-sharing $(Sn^{4+})S_6$ octahedra (CN = 6) capped at the extremities by two Pb^{2+} cations, which exhibit a tetrahedral coordination PbS_3L (L being the Pb^{+2} lone pair electrons), forming $[Sn_2Pb_2S_6]$ chains that run parallel to the *b*-axis (**Figure 1a**). The crystal structure can be described as an ABAB stacking along the *c*-axis of $[Sn_2Pb_2S_6]$ chains and displayed as layers packed along the *a*-axis in which the alignment of the columns alternates between the planes (103) and (-103) **(Figure S1, Supporting Information, SI)**.[42] Hence, the 1D crystal structure of $PbSnS_3$ can be represented by $[Sn_2Pb_2S_6]$ chains, characterized by strong intrachain Sn-S (2.56 to 2.63 Å) and Pb-S (2.78 to 2.94 Å) ionocovalent bonds, interconnected by weak interchain Pb···S interactions (3.08 Å to 3.41 Å), as shown in **Figure 1a** and **Figure S2, SI**.

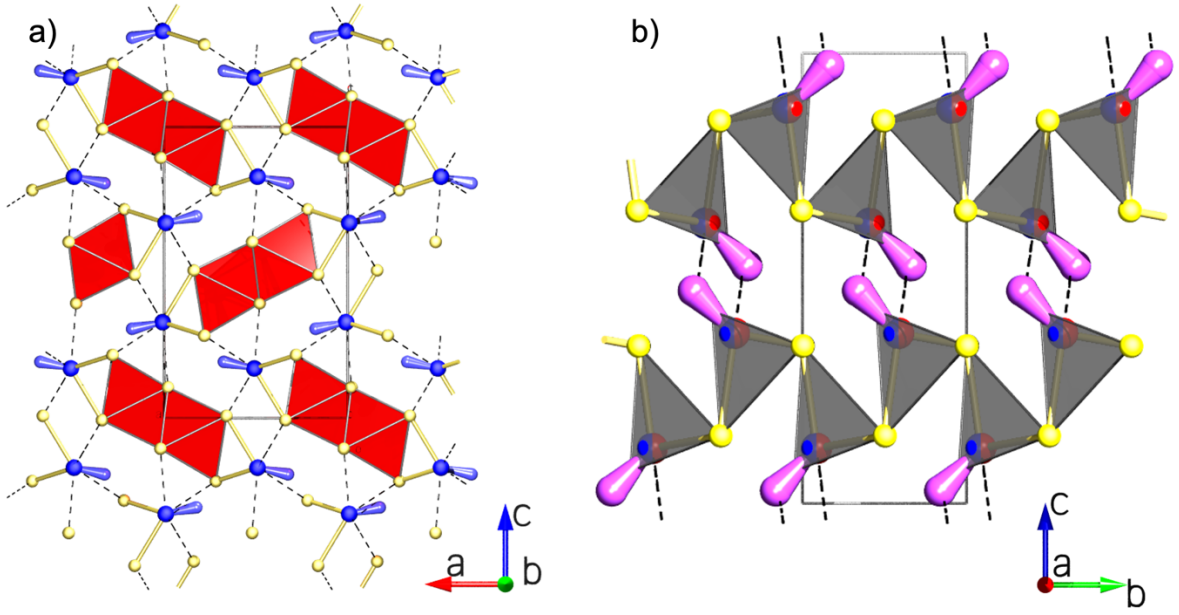

Figure 1. a) Crystal structure representation of 1D $PbSnS_3$ (space group *Pnma*). Double columns of edge-sharing $(Sn^{4+})S_6$ octahedra (red) capped at the extremities by two Pb^{2+} cations (blue), forming $[Sn_2Pb_2S_6]$ chains running along the *b*-axis. The lone pair electrons of Pb^{2+} is illustrated in blue color and weak interchain Pb···S interactions (3.08 Å to 3.41 Å) are represented as dashed lines. b) Crystal structure representation of 2D $PbSnS_2$ (space group *Pmcn*). (Pb,Sn)S_3L tetrahedra, represented in dark grey, form chains oriented along the *b*-axis. The lone pair electrons (L) of Pb^{2+} (blue) and Sn^{2+} (red) cations, statistically distributed on the same crystallographic site, are represented in pink. Weak interlayer interactions between Pb^{2+}/Sn^{2+} cations of two consecutive layers and their lone pairs are represented as dashed lines. S atoms are shown in yellow. Approximate positions of the lone pairs are represented with sphere-capped cones stemming from Pb/Sn atoms.

$PbSnS_2$, known as mineral teallite,[43] corresponds to the $x = 0.5$ composition in the $Pb_xSn_{1-x}S$ solid solution, where complete miscibility of Pb and Sn was reported in the range $0 \leq x \leq 0.55$.[44-46] In this composition range, the compounds crystallize in the herzenbergite (SnS) orthorhombic structure (space group *Pmcn*, the 5th setting of space group *Pnma*, No 62), with Pb and Sn atoms located on the same crystallographic site.[47, 48] Note that the existence of a superstructure in $PbSnS_2$, due to the ordering of Pb and Sn atoms, is still a matter of debate for more than 50 years.[45] Herzenbergite is conventionally described as a two-dimensional structure

built up of strongly distorted rock salt slabs in the *ab*-plane, that are stacked along the *c*-direction.[46, 47] However, such a description is misleading, since besides expected normal (Pb^{2+}, Sn^{2+})-S bonds, it involves (Pb, Sn)-S distances of about 3.50 Å that are much larger than the sum of ionic radii.[49] Bearing in mind that, in $PbSnS_2$, each Sn^{2+}/Pb^{2+} cation exhibits a tetrahedral coordination PbS_3L or SnS_3L similar to that observed for Pb^{2+} in $PbSnS_3$, we can describe the 2D crystal structure of $PbSnS_2$ (**Figure 1b)** as the stacking along the *c*-axis of puckered [$PbSnS_2$] layers built up of corner-sharing $(Pb,Sn)S_3L$ tetrahedra. The intralayer (Pb,Sn)-S distances, ranging from 2.59 to 2.73 Å, indicate strong ionocovalent (Pb,Sn)-S bonds, similar to the intrachain Pb-S distances in the 1D $PbSnS_3$. However, compared to $PbSnS_3$ for which the interlayer (Pb/Sn)-S distances are all greater than 3.5 Å, the Pb/Sn-L--Pb/Sn distances between the layers are rather short ~3.47 Å, indicating that the lone pair L of one layer stays at about 2.5 Å from the Pb^{2+} (or Sn^{2+}) cation of the next layer. This strongly suggests that the cohesion of the structure of $PbSnS_2$ is ensured by very weak interlayer interactions between the Pb^{2+} or Sn^{2+}cations of two consecutive layers via their lone pair L, *e.g*. Pb-L···Pb or Sn-L···Sn, or Pb-L···Sn or Sn-L···Pb interactions (**Figure 1b**).

To understand the nature of chemical bonding in these two compounds, representation of their total electronic charge densities, obtained from density functional theory (DFT) calculations, are shown in **Figure 2a and 2b** for $PbSnS_3$ and $PbSnS_2$, respectively. Due to the difficulties to calculate structure with partial occupation, a structural model with cationic ordering $Pmc2_1$ was considered in accordance with the literature.[39, 50, 51] The strong directional overlap of charge clouds between Sn and S atoms highlights the covalent part of chemical bonding, despite the different oxidation state of Sn in the two compounds (see below). For 2D $PbSnS_2$, it signifies strong covalent intralayer bonds without overlapping of charges between two consecutive layers, confirming our description of the layered structure of this material, with weak (Pb,Sn)···(Pb,Sn) interlayer interactions via the lone pair of the Pb^{2+}/Sn^{2+} cations, as described above. Concerning 1D $PbSnS_3$, the charge overlapping between Pb and S is not uniform across all nearest-neighbour Pb-S pairs due to their varying bond-lengths, as shown in **Figure S2, SI**. More importantly, it highlights the absence of charge overlapping in some directions indicating the absence of strong interactions between $[Sn_2Pb_2S_6]$ chains, probably related to the much longer interchain Pb···S distances (3.08 Å to 3.41 Å), suggesting a delocalization of the lone pair of electrons of Pb^{2+}.

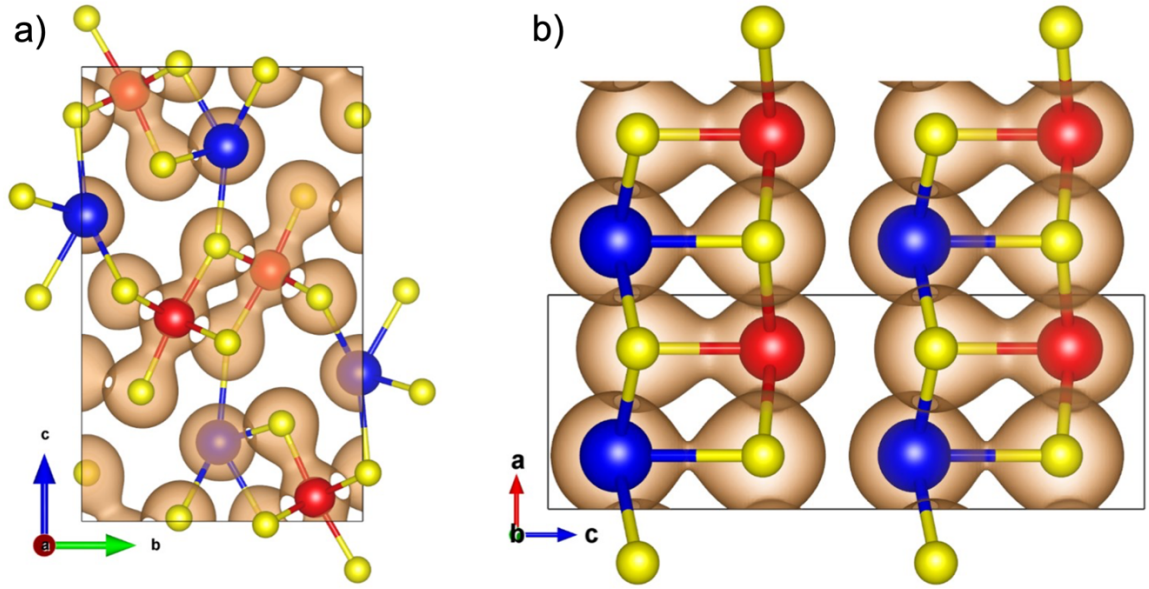

Figure 2. DFT-calculated total charge density (iso-surface value 0.045 e/bohr^3) of a) $PbSnS_3$ and b) $PbSnS_2$. Pb, Sn and S atoms are depicted in blue, red and yellow, respectively.

Synthesis and structural analysis of the samples

Polycrystalline $PbSnS_3$ and $PbSnS_2$ samples were synthesised via high-energy ball milling followed by spark plasma sintering at 723 K (see experimental methods in SI for details). Powder X-ray diffraction (PXRD) patterns of $PbSnS_3$ and $PbSnS_2$ samples are well indexed with the orthorhombic unit cells reported for suredaite (space group $Pnma$, No 62) and herzenbergite (space group $Pmcn$, the 5th setting of space group $Pnma$, No 62) minerals, respectively, as displayed in **Figure 3a and 3b**.

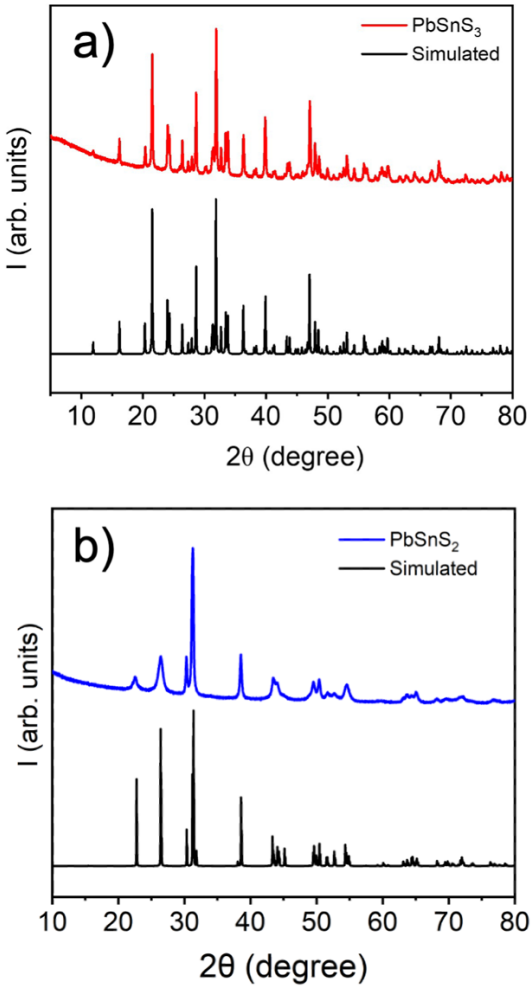

Figure 3. PXRD patterns (λ = 1.5406 Å) of a) $PbSnS_3$ and b) $PbSnS_2$ samples.

Sharp diffraction peaks in $PbSnS_3$ show the high crystallinity of the sample and the absence of structural defects (see Rietveld refinement of PXRD data in **Figure S3** and **Table S1a, SI**). The refined lattice parameters of a = 8.7108(2) Å, b = 3.7920(1) Å, and c = 14.0681(2) Å are in good agreement with literature.[41] PXRD also reveals the presence of (Pb,Sn)S impurity (rock salt structure) in weak proportion (< 2 wt.%, Figure S3, SI). To study our sample on a smaller length scale, we also carried out a structural analysis using precession-assisted 3D electron diffraction (3D ED) in a TEM. 3D ED[52] makes it possible to acquire diffraction data from a single crystal smaller than 100 nm. Thanks to an ever-increasing improvement in data acquisition and processing, 3D ED can provide a highly accurate picture of the structure of materials with small crystalline domains. For $PbSnS_3$, 3D ED shows that the structure of an individual crystal/grain is not different from that obtained by PXRD (see **Table S1b, SI)**. With the ability to refine the atomic displacement parameters (ADPs) using an anisotropic model, we

also find that there are no anomalies in the ADPs that indicates the absence of positional disorder. Bond valence sum (BVS) calculations based on our structural analyses by PXRD and 3D ED (**Table S1**, **SI**) show that the structure is compatible with the existence of oxidation states +II and +IV for Pb and Sn, respectively. Further TEM analyses confirm the high crystallinity of $PbSnS_3$ sample (**Figure 4a-e**). The high-angle annular dark-field image (HAADF) is well indexed to the [001] zone of $PbSnS_3$ (*Pnma*) as shown in **Figure 4c, 4e.** The atomic projection along [001] zone is displayed in **Figure 4d**. The bright spots in the HAADF image correspond to the Pb and Sn columns due to their large atomic number (also see the overlaid atomic structure). Note that $PbSnS_3$ has uniform grains of ~100 nm in size (**Figure 4a**). The chemical analysis from EDS mapping shows that Pb, Sn and S are uniformly distributed except for some minor Pb-rich impurities, as shown in **Figure 4b**, that could correspond to the (Pb,Sn)S phase detected by PXRD**.**

In addition to PXRD and TEM analyses, we have performed ^{119}Sn Mossbauer spectroscopy measurements at 15 K to determine the oxidation states of Sn and to analyse its chemical environment in both $PbSnS_2$ and $PbSnS_3$ samples. Mössbauer spectrum recorded on $PbSnS_3$ sample shows a relatively broad single peak centered at 1.14(1) mm.s^{-1}, indicating that Sn atoms are in their +IV oxidation state and in octahedral environment of sulphur.[53-55] This Mössbauer spectrum can be refined by considering a doublet with a quadrupole splitting of 0.41(1) mm.s^{-1} and a FWHM of 0.87(1) mm.s^{-1} (**Table S3** and **Figure S4, SI**). These values are in fair agreement with those reported by Greatrex *et al*. on this compound.[54]

PXRD pattern of $PbSnS_2$ exhibits broad diffraction peaks except for some specific reflections suggesting microstructural effects. The pattern has been fitted considering different physical models describing anisotropic peak broadening. However, they led systematically to poor agreement between simulated and experimental patterns. Indeed, the Stephen's method[56] used for anisotropic strain was unable to reproduce the broadening, with anisotropic size broadening converging to unphysical shapes (cross-like) of the crystallites that are not compatible with TEM microscopy (see below). It is worth considering that size-like peak selective broadening observed here is a signature of the existence of crystallographic defects, such as antiphase domains or stacking faults, which have been reported as common defects in teallite $PbSnS_2$.[57] In a first approximation, if defects are only antiphase domain, the structure factors should not be affected and, as a consequence, the microstructure could be taken into account in the Rietveld treatment by using two groups of *hkl* reflections (in our case, *hkl* reflections with $h=k$ or $h\neq k$) and refining different half width parameters for each group. Using

this approximation, a relatively good agreement between the experimental and theoretical patterns is obtained (**Figure S5, SI**). However, the ADPs are relatively low (**Table S2, SI**) and impossible to refine independently. The cell parameters converge toward a pseudotetragonal structure (a = 4.1511(1) Å, b = 4.1769(2) Å, c = 11.4533(2) Å), with lattice parameters different compared to those reported in synthetic compounds prepared by sealed tube synthesis or in natural tealite minerals with the same composition $PbSnS_2$ (a ~ 4.09 Å, b = 4.27 Å, c = 11.42 Å).[44, 46, 47] The situation is here different from the point of view of 3D ED since we obtain a much more marked difference between the a and b parameters (a = 4.069(2) Å, b = 4.275(3) Å, c = 11.474(9) Å). Although the accuracy of cell parameters determination has improved considerably,[58] 3D ED is not as accurate as PXRD. Nevertheless, we note that the cell parameters obtained by 3D ED are in close agreement with those in the literature. In the case of 3D ED, it was possible to achieve a structure refinement including anisotropic ADPs for each atomic position (**Table S2, SI**). While the picture of the $PbSnS_2$ structure obtained by 3D ED seems acceptable, one point of concern should be mentioned. The U33 ADP for the S1 position (**Table S2, SI**) shows an anomaly with a zero value, given the uncertainty. This might point towards a static disorder for this position, related to the existence of a slightly different structure at an atomic scale.[51] As mentioned earlier, several models have been proposed for $PbSnS_2$ involving local Pb/Sn ordering and correlated S displacements. Regarding Bond Valence Sum (BVS) calculations, the mixed Pb/Sn atomic position is, as averaged, compatible with the existence of an oxidation state of +II for both Sn and Pb. Mössbauer spectrum of $PbSnS_2$ sample, shown in **Figure S4**, **SI** evidences a doublet centered at 3.31(1) $mm.s^{-1}$, confirming a +II oxidation state of Sn atoms in environment of sulphur.[53, 59] The values of the isomer shift and refined quadrupole splitting (**Table S3, SI**) are in agreement with the results reported by de Kergommeaux *et al*.[59] on isostructural nanocrystalline SnS samples. In addition to the doublet, a weak intensity peak centered at 0.06(1) $mm.s^{-1}$ is observed and, considering its isomer shift and refined quadrupole splitting,[60] can be attributed to SnO_2 impurity (~3 % according to the refinement, **Table S3, SI**).

The difference between the results obtained by 3D ED and PXRD with, in the latter case, a pseudo-tetragonal cell and peak broadenings, might be explained by the presence of small crystalline domains and subtle changes in the local structure, possibly involving local ordering or stacking faults. This has to be related to the method of synthesis (temperature, reactivity, quenching...) and also to the flexibility of SnS structural type, in which the local distortions associated with Pb in the $Sn_{1-x}Pb_xS$ ($x \leq 0.55$) solid solution are probably compensated by a

significant reduction of orthorhombicity. To get an insight into the microstructural features in $PbSnS_2$ and understand this difference, local TEM analysis has been performed. It first demonstrates that the crystallite/grain morphology is quite distinct from that of $PbSnS_3$. First, $PbSnS_2$ sample shows larger grain size (mainly 200-300 nm) with strip-like grains (**Figure 4f**). In addition, the EDS mapping (**Figure 4g**) indicates a uniform chemical distribution of the elements. The good consistency between the [110] atomic projection (**Figure 4j**) and HAADF image (**Figure 4k**) demonstrates that the crystal structure of $PbSnS_2$ is coherent with the SnS-like structure.[37, 39] The uniform contrast in HAADF (**Figure 4k**) suggests a random occupation of Pb and Sn in the cationic sites. The dense elongated fringes shown in **Figure 4f** indicate the presence of planar/lamella-like defects in $PbSnS_2$ sample. Indeed, **Figure 4h** shows the appearance of "twisted lamellas" inside the "grain" view along the [110] direction, which should contribute to the elongated lattice fringes. The "twisted lamellas" are domains appearing slightly rotated around the *c* axis (inset **Figure 4i and top part Figure 4i**). Thus, the "grains" are divided into several small pieces by these "twisted lamellas" and boundaries, as seen in the inserted images in **Figure 4h.** Field emission scanning electron microscopy-back scattered electron (FESEM-BSE) shows the phase purity of the samples ($PbSnS_3$, **Figure S6a, SI**; $PbSnS_2$, **Figure S7a, SI**) without any secondary phase. Further corresponding energy-dispersive X-ray (EDX) demonstrated the uniform distribution of Pb, Sn and S in $PbSnS_3$ (**Figure S6b-d, SI**) and $PbSnS_2$ (**Figure S7b-d, SI**).

These pieces of information coming from PXRD and TEM analyses suggest a particular stacking fault defect already observed for tealite film[61] in which the crystal is composed of alternating domains with an orientation of the slab rotated at ~90°. Such defect could be depicted as a pseudo-merohedrical twinning (generation of a pseudo-mirror), with the small misorientation Δ along the [001] direction (**Figure S8, SI**)[62] being directly dependent on the degree of orthorhombicity of the unit cell, i.e. a few degrees for a typical tealite structure. In particular, such a kind of defects justifies the "pseudo-tetragonality" observed from refined PXRD data and the orthorhombicity observed by 3D ED local analysis. Note that the simultaneous presence of domains with different orientations favors the reduction of orthorhombicity to a pseudotetragonal symmetry, as already seen for different systems.[63] In our $PbSnS_2$ sample, the combination of mechanical alloying and SPS at relatively low temperatures is functional to the appearance of such structural defects leading to the "pseudo-tetragonality". To confirm this hypothesis, we have annealed a $PbSnS_2$ mechanically-alloyed powder sample (see PXRD in experimental section) in a sealed tube at 873 K for 24h (heating and cooling of

6h), *i.e.* above 800 K, where the phase transition from the lower symmetric *Pmcn* (or *Pnma*) phase to the higher symmetric *Cmcm* phase occurs in SnS[64] and $PbSnS_2$.[39] The PXRD pattern of this annealed sample **(Figure S9, SI)** confirms without any ambiguity that the cell parameters change to a more orthorhombic symmetry with lattice parameters of a = 4.0960(1) Å, b = 4.2579(1) Å, c = 11.4556(2) Å, in accordance with the ones commonly reported in literature.[44, 46, 47] In addition to this, the selective strong peak broadening disappears. In the annealed powders, all reflections are much sharper presenting broadening comparable to the narrowest reflections of the SPS sample. The unit cell volume (199.241(3) $Å^3$ in annealed powder against 198.587(11) $Å^3$ in sintered sample) is almost unchanged, excluding any possibility of composition change during annealing. This confirms our conclusion that the low orthorhombic distortion observed in the structure of our bulk $PbSnS_2$ sample, *i.e.* its pseudotetragonality, is directly related to the existence of small crystalline domains with structural defects which are formed due to the low-temperature synthesis conditions (mechanical-alloying + SPS at 723 K).

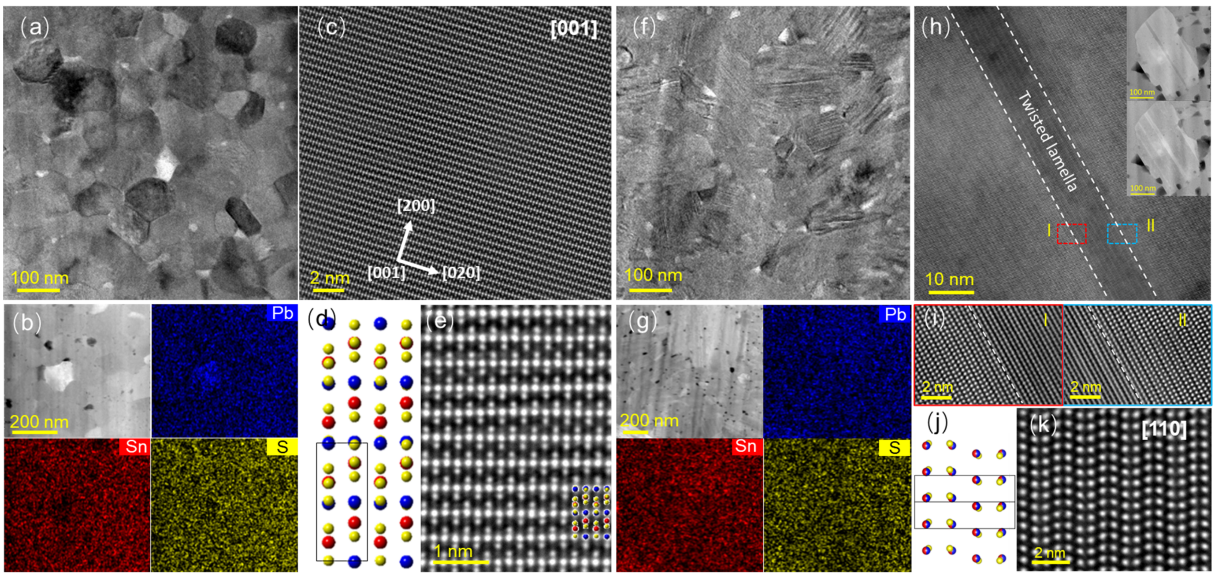

Figure 4. TEM characterizations of $PbSnS_3$ (a-e) and $PbSnS_2$ (f-k) samples. (a) Morphology, (b) EDS mapping, (c) HAADF image, (d) [001] atomic projection and (e) corresponding atomic-resolved HAADF image of $PbSnS_3$. (f) Morphology, (g) EDS mapping, (h) HAADF image (j) [110] atomic projection and (k) corresponding HAADF image of $PbSnS_2$. The insets show the low-magnification view of (h) with different sample tilting angles. (i) Enlarged views highlighting regions with boundaries in (h). The Pb, Sn and S atoms in the structural models (d) and (j) are represented by blue, red and yellow balls, respectively.

We have measured the thermal conductivity of $PbSnS_3$ and $PbSnS_2$. Note that the low electrical conductivity of the $PbSnS_3$ sample ($\sigma < 10^{-6}$ S/cm) does not allow to measure the

electrical conductivity using ZEM-3 apparatus which indicates the insulating nature of the sample. Thus, electrical contribution to the thermal conductivity is negligible, making the phonon contribution the dominant source of heat propagation. $PbSnS_2$ has a higher electrical conductivity (**Figure S10a, SI**) of 5×10^{-4} S/cm at ~ 473 K but still sufficiently small to neglect the electronic contribution to κ. The high resistivity of both samples is further supported by the large optical band gap (**Figure S11, SI**) measured for both compounds. $PbSnS_2$ exhibits *n*-type electrical conduction (electrons are major carriers) as the magnitude of the Seebeck coefficient is negative with a value as high as -1100 μV/K at ~ 473 K, as shown in **Figure S10b, SI.**

At low temperatures, the κ_L of $PbSnS_3$ increases with increasing temperature to reach a maximum, known as the Umklapp peak, at 77 K with a value of 1.7 W/m.K (**Figure 5a**). Upon further warming, κ_L further decreases to reach values in the range of 1~0.8 W/m.K between 300 and 673 K. The upturn in thermal conductivity data at high temperature could be due to the contribution from the electronic thermal conductivity.

The behavior of the κ_L of $PbSnS_2$, in the temperature range from 2 to 673 K, is quite different compared to $PbSnS_3$ or other conventional crystalline materials. In a typically crystalline material like $PbSnS_3$, κ_L exhibits an Umklapp peak (~77 K) followed by a decrease following a T^{-1} dependence due to Umklapp scattering. Conversely, κ_L of $PbSnS_2$ increases up to 100 K and then becomes nearly constant between 100 and 673 K (**Figure 5a**) lacking an Umklapp peak. Moreover, the κ_L value at 300 K is equal to 0.6 W/m.K, i.e. lower than values reported for PbS and SnS, as well as for other *state-of-the-art* low thermal conductive metal sulphides as shown in **Figure S12, SI.** Although $PbSnS_2$ can be viewed as a solid solution between PbS and SnS in equal proportion, the induced mass and strain field fluctuations, estimated by the Klemens-Callaway model, do not entirely account for the decrease of κ_L from 1.4 W/m.K in SnS to 0.6 W/m.K in $PbSnS_2$ (see SI for the equations). The most noteworthy observation is the unusual amorphous or glass-like thermal conductivity. A similar type of thermal conduction behavior has been recently observed in $BaTiS_3$,[65] WSe_2,[66] $Bi_4O_4SeCl_2$,[5] and $Cs_3Bi_2I_6Cl_3$.[67]. The estimated values of the theoretical minimum lattice thermal conductivity, $\kappa_{min,}$ and diffuson lattice thermal conductivity, κ_{diff}, for $PbSnS_2$ are 0.35 W/m.K and 0.21 W/m.K, respectively (**Table S4, SI**). To further clarify the origin of low κ_L in $PbSnS_2$, we have measured the thermal conductivity (**Figure S13, SI)** of the well-crystallized annealed sample (see structural section)**.** The results shows that κ_L of both the samples (non-annealed and

annealed) are quite similar, indicating that the defects observed in the non-annealed sample have a negligible effect on κ_L in $PbSnS_2$.

To understand the low κ_L in these compounds, we have studied the low-temperature heat capacity (C_p) in the temperature range of 2-50 K, as shown in **Figure S14, SI.** We have fitted our data using Debye-Einstein (three Einstein modes) model as a single Debye model is not sufficient to fit the data. The C_p/T *vs* T^2 plot of $PbSnS_3$ and $PbSnS_2$ is shown in **Figure 5b** and **5c**, respectively, which is well fitted using the following equation:[17, 68]

$$\frac{C_p}{T} = \gamma + \beta T^2 + \sum_n \left(A_n \left(\theta_{E_n}\right)^2 . (T^2)^{-3/2} . \frac{e^{\theta_{E_n}/T}}{\left(e^{\theta_{E_n}/T} - 1\right)^2} \right)$$

where the first term in the equation γ (Sommerfeld constant) denotes the electronic contribution, and β denotes the lattice contribution. The third term in the equation consist of Einstein oscillator where A_n and θ_{E_n} are the prefactor and Einstein temperature of the n^{th} oscillator mode. Our fitted data shows that three Einstein temperatures are 21 K (15 cm^{-1}), 55 K (38 cm^{-1}) and 99 K (69 cm^{-1}) for $PbSnS_3$, whereas, for $PbSnS_2$, the three Einstein temperatures are 18 K (12 cm^{-1}), 52 K (36 cm^{-1}) and 93 K (65 cm^{-1}) as mentioned in **Table S5, SI**. These low energy optical phonon modes can be attributed to the thermal vibrations of Pb atoms and to some extent Sn atom vibrations (discussed below) based on calculations of the phonon density of states (**Figure S15, S16, SI**). **Figure 5b and 5c** inset show the presence of a pronounced peak at ~10 K in C_p/T^3 vs T plot for $PbSnS_3$ and $PbSnS_2$, respectively. This peak is a signature of the presence of excess optical phonon modes at low energy, which interact with the heat carrying acoustic phonon modes and result in a low κ_L in both compounds.[69] The sound velocity provides information about the energy of the heat carrying acoustic phonon modes (slope of acoustic phonon dispersions).[70] The measured longitudinal, transverse, and average sound velocities for $PbSnS_3$ ($PbSnS_2$) are 3375 m/s (2930 m/s), 1402 m/s (1288 m/s) and 1586 m/s (1454 m/s), respectively (**Table S4, SI**). These low speeds of sound are one of the reasons why κ_L for both compounds is very low.

To comprehend the different phonon mechanism in thermal conductivity data, we have fitted our experimental data using the Debye–Callaway model (**Figure 5d**).[71]

$$\kappa_L(x) = \frac{k_B}{2\pi^2 v_a} \left(\frac{k_B T}{\hbar}\right)^3 \int_0^{\frac{\theta_D}{T}} \frac{x^4 e^x}{\tau_{ph}^{-1} (e^x - 1)^2} dx$$

where *x* is defined as $\frac{\hbar\omega}{k_B T}$ ($\hbar$: reduced Planck constant, (ω: phonon angular frequency) τ_{ph} is the phonon scattering relaxation time. The scattering rate can be expressed as $\tau_{ph}^{-1} = \tau_B^{-1} + \tau_D^{-1} + \tau_U^{-1}$ (boundary scattering, $\tau_B^{-1} = \frac{v_a}{L}$, point defect scattering, $\tau_D^{-1} = A\omega^4$ and Umklapp scattering, $\tau_U^{-1} = B\omega^2 T e^{\frac{-\theta_D}{mT}}$ where v_a is the sound velocity, θ_D is Debye temperature, *L* is the grain size, m is the dimensional constant, *A* and *B* are fitting parameters). All these parameters are mentioned in **Table S6, SI.** The phonon relaxation time for the different scattering mechanisms is depicted in **Figure 5e.** The trend indicates that Umklapp scattering (intrinsic effect), with a shorter phonon relaxation time, dominates compare to defect scattering (extrinsic effect) for the reduction of κ_L .

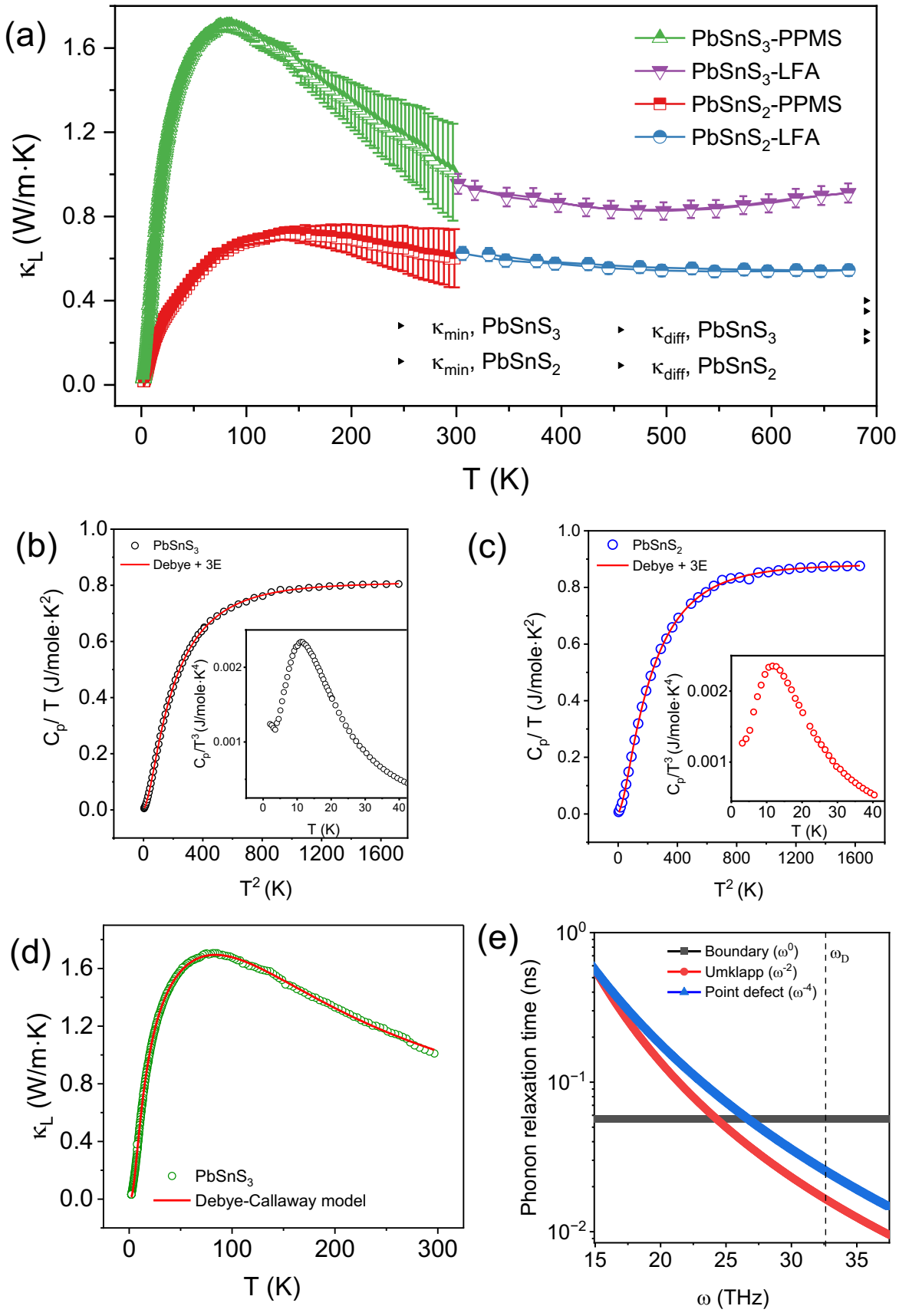

Figure 5. (a) Temperature-dependent lattice thermal conductivity (κ_L) of $PbSnS_3$ and $PbSnS_2$ measured using PPMS (2–300 K) and LFA (300–673 K). κ_{min} stands for the theoretical

minimum value of κ_L while κ_{diff} is the diffusive minimum thermal conductivity. Low temperature C_p/T versus T^2 plot of (b) $PbSnS_3$ and (c) $PbSnS_2$ with fits with the Debye–Einstein model. Inset shows the presence of a pronounced peak in C_p/T^3 vs T plot. (d) Thermal conductivity data of $PbSnS_3$. The red solid line shows the fit to the data with the Debye–Callaway model. (e) Calculated phonon relaxation time, for different scattering mechanisms involved in the lattice thermal conductivity, as a function of frequency, where ω_D is the Debye pulsation.

We have performed first principle DFT calculations to analyse the chemical bonding and lattice dynamics of $PbSnS_3$ and $PbSnS_2$ to shed further light on the origin of the low κ_L. In $PbSnS_3$, Pb and Sn ions have oxidation states of +II and +IV, respectively, as shown by ^{119}Sn Mössbauer spectroscopy, leaving a lone-pair electrons only on Pb^{2+} cations i.e., the $6s^2$ lone-pair. On the other hand, in $PbSnS_2$, both Pb and Sn have +II oxidation states, leaving lone-pairs electrons on both Pb^{2+} ($6s^2$) and Sn^{2+} ($5s^2$) cations. These latter can induce strong anharmonicity, which in turn can significantly enhance the phonon-phonon scattering rates and hence, reduce the lattice thermal conductivity.[72, 73] We plot the orbital resolved electronic density of states (DOS) for Pb and Sn atoms separately for $PbSnS_3$ (**Figure 6a, 6b**) and $PbSnS_2$ (**Figure 6d, 6e**) to reveal the presence of the lone-pairs near the Fermi level (E_F). For $PbSnS_3$, the Pb $6s^2$ lone-pair (**Figure 6a**) has a broad contribution between -2 to 0 eV just below E_F as compared to the Pb $6s^2$ lone-pair in $PbSnS_2$ which is sharply localized around -1 eV (**Figure 6d**) below E_F. A broad distribution of Pb $6s^2$ lone-pair in $PbSnS_3$ indicates its partial hybridization with other orbitals (see atom resolved DOS, **Figure S17, SI**). Interestingly, owing to the +IV oxidation state of Sn in $PbSnS_3$, it does not have a contribution of Sn $5s^2$ lone-pair electrons just below E_F (**Figure 6b**) whereas, in $PbSnS_2$, Sn shows a sharply localized $5s^2$ lone-pair just around -0.5 eV below E_F (**Figure 6e and S18, SI**). The sharp localization of the lone-pair electrons on Pb^{2+} and Sn^{2+} in $PbSnS_2$ signifies their stereochemical activity. Based on the partial electronic DOS and chemical bonding analysis, we present schematics of molecular orbital (MO) diagrams for $PbSnS_3$ (**Figure 6c**) and $PbSnS_2$ (**Figure 6f**). The MO diagrams show that both compounds and especially $PbSnS_2$ have filled antibonding states below E_F, which makes both compounds elastically soft, in agreement with the low speeds of sound measured **(Table S4, SI)**. To further confirm the presence of lone-pair electrons, we calculated the electron localization function and plotted in **Figure 6g** ($PbSnS_3$) and **Figure 6h** ($PbSnS_2$). These results show that the charge densities on Pb^{2+} for $PbSnS_3$ and on Pb^{2+} and Sn^{2+} for $PbSnS_2$ are asymmetric, corresponding to their lone-pair of electrons. The spherical charge cloud on S atoms is due to its -II oxidation state which does not correspond to a lone-pair of electrons. For

both compounds, the lone-pair of electrons on Pb^{2+} and Sn^{2+} are localized on a side which otherwise would have an interaction with the neighboring S atom. The electron lone-pairs on Pb^{2+} and Sn^{2+} atoms in $PbSnS_2$ face towards each other (**Figure 6h**), providing a strong electrostatic repulsion which distorts the coordination environment. This distortion is expected to make $PbSnS_2$ relatively more anharmonic than $PbSnS_3$. Finally, to confirm the presence of anti-bonding states, we performed the Crystal Orbital Hamilton Population (COHP)[74] analysis in $PbSnS_3$ (**Figure 6i**) and $PbSnS_2$ (**Figure 6j**). The COHP analysis reveals that $PbSnS_2$ has a much larger antibonding states just below E_F (between -2 eV to 0 eV) compared to that of $PbSnS_3$, which is primarily due to Sn-S interactions that is induced by the stereo chemically active $5s^2$ lone-pair electrons of Sn^{2+}. The presence of filled antibonding states weakens the chemical bond strength[75] and phonon group velocity which induces very low κ_L (Please see SI for details).[75, 76] Thus, $PbSnS_2$ is expected to exhibit lower κ_L than $PbSnS_3$. We have further calculated the second order interatomic force constant (IFC). The Pb-S and Sn-S bonds in $PbSnS_2$ has a lower second order IFC value than the Pb-S and Sn-S bonds in $PbSnS_3$ (**Figure S19, SI**), which is due to the presence of more pronounced antibonding states just below the Fermi level in $PbSnS_2$. The existence of a weak second order IFC value further supports the lower κ_L in $PbSnS_2$ with respect to $PbSnS_3$.

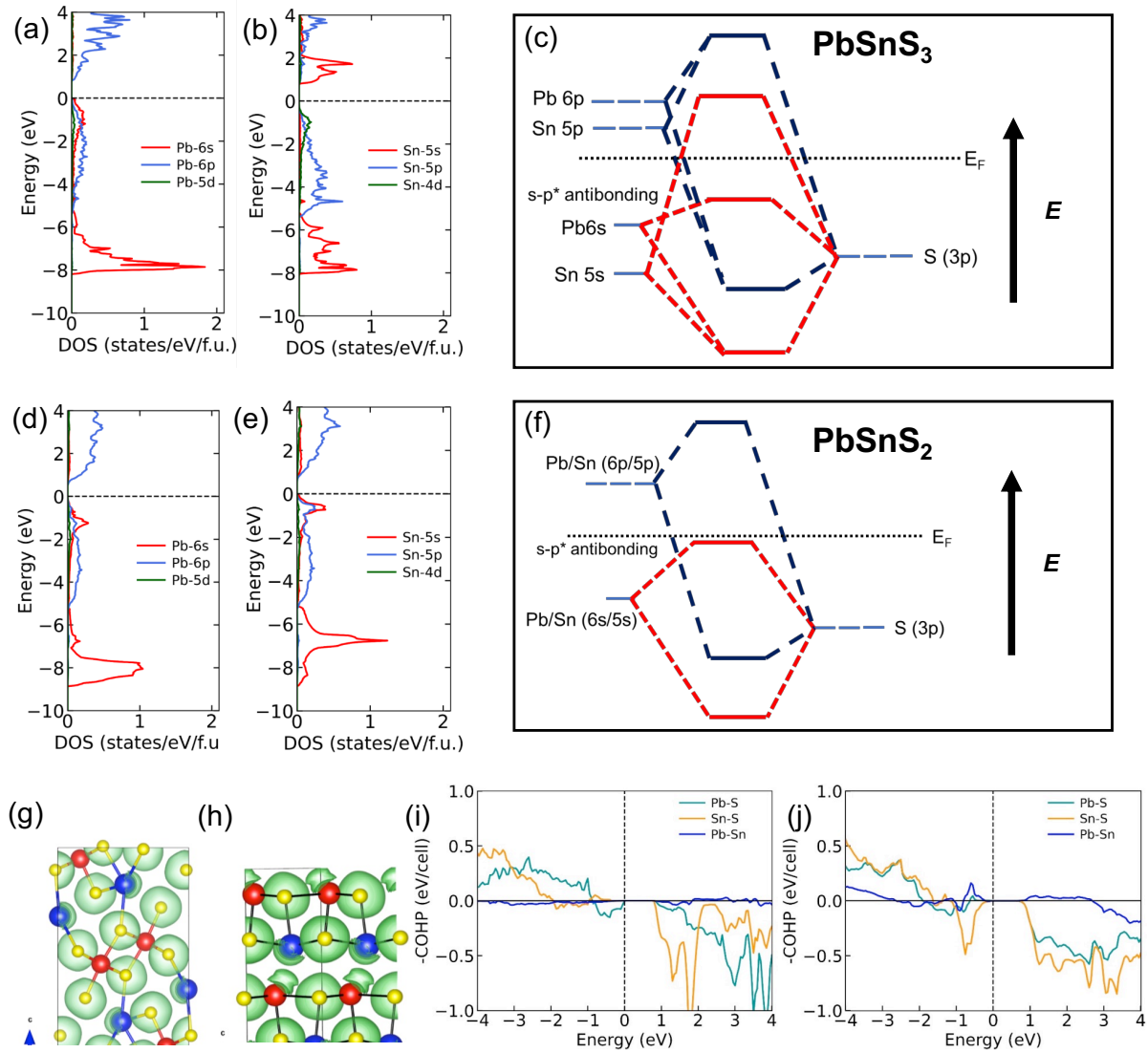

Figure 6. Orbital-resolved partial electronic density of states for the Pb and Sn atoms in $PbSnS_3$ (a, b) and $PbSnS_2$ (d, e). Schematics of the molecular orbital diagrams for (c) $PbSnS_3$ and (f) $PbSnS_2$ as deduced from the partial density of states and chemical bonding analysis. Visualizations of the electron localization function (plotted with an iso-surface value which is 55% of the maximum) for (g) $PbSnS_3$ and (h) $PbSnS_2$. Pb, Sn and S atoms are depicted in blue, red and yellow, respectively. The Crystal Orbital Hamilton Population (COHP) analysis for (i) $PbSnS_3$ and (j) $PbSnS_2$.

The calculated phonon dispersions for $PbSnS_3$ (**Figure 7a**) and $PbSnS_2$ (**Figure 7d**) exhibit very soft acoustic phonon branches with frequency below 40 cm^{-1} in all directions in the Brillouin zone that give rise to very low speeds of sound in agreement with the experimental results **(Table S4, SI)**. These low speeds of sound are one of the reasons why κ_L for both compounds are very low. In addition, phonon dispersions for both compounds exhibits several weakly-dispersive, low-energy (< 60 cm^{-1}) optical phonon branches (**Figure 7a and 7d**). The atom-resolved phonon density of states (**Figure 7b and 7e**) reveal that these dispersionless

phonon branches give rise to the strong localization of phonon modes in a narrow energy window around 40 cm^{-1}, particularly the contributions coming from the Pb atoms. These weakly dispersive and low-energy phonon branches are expected to give rise to numerous phonon-scattering events that strongly suppress lattice thermal conductivity in crystalline materials, inducing ultralow κ_L.[77, 78]

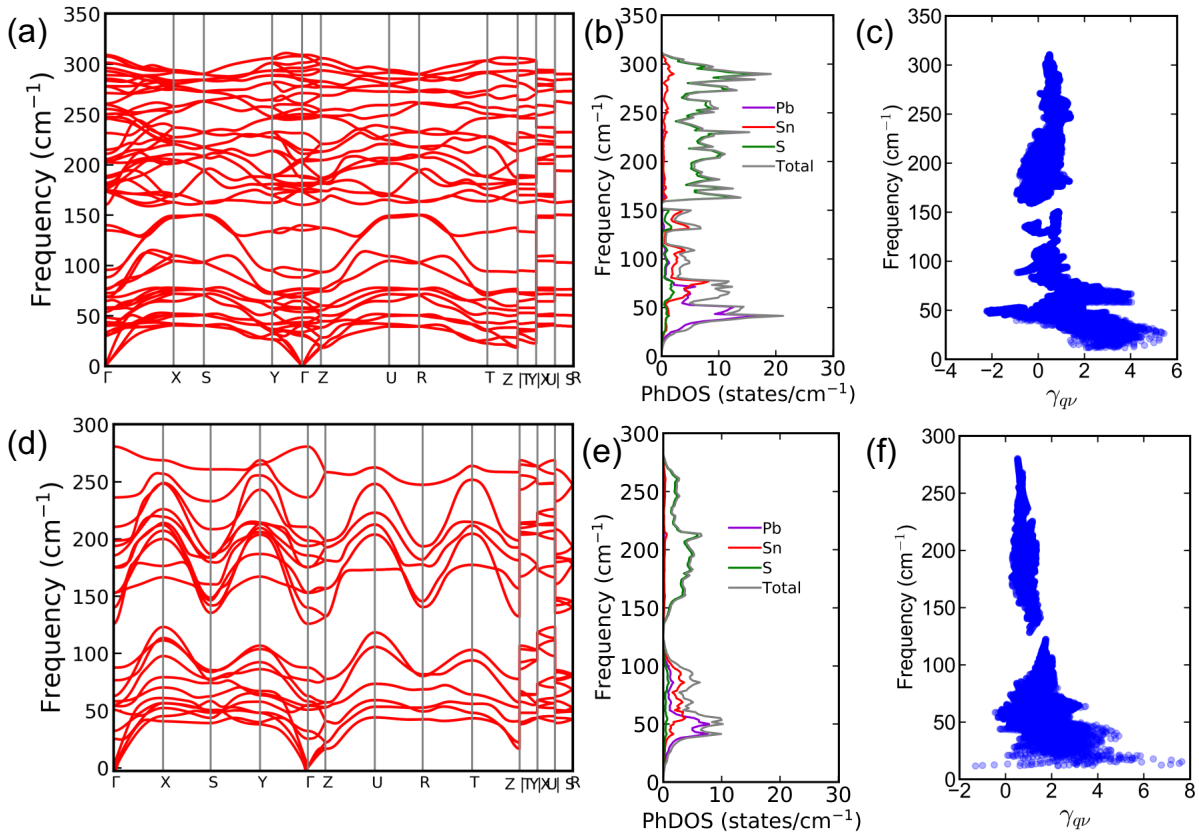

Figure 7. (a) Phonon dispersion, (b) atom-resolved phonon density of states, and (c) mode Gruneisen parameters for $PbSnS_3$. The same for $PbSnS_2$ in (d), (e), and (f), respectively.

Due to the stereo chemically active lone-pairs of Pb^{2+} and Sn^{2+}, we expect the phonon modes of $PbSnS_3$ and $PbSnS_2$ to be anharmonic. To quantify their strength, we have calculated the mode Gruneisen parameters ($\gamma_{q\upsilon}$) which are shown in **Figure 7c** ($PbSnS_3$) and **Figure 7f** ($PbSnS_2$). Very high values (>> 1) of ($\gamma_{q\upsilon}$) are evidenced for the acoustic and low-energy optical phonons. We can also see that, for the low-energy phonon modes (< 60 cm^{-1}), some of the mode Gruneisen parameters of $PbSnS_2$ are larger than $PbSnS_3$. Since the phonon scattering rates increase with the inverse square of ($\gamma_{q\upsilon}$),[73] the observation of ultralow κ_L in both compounds is expected. Therefore, strong phonon anharmonicity and antibonding valence bands induced by the lone-pair electrons, low speeds of sound, and localized low-energy phonon modes

rationalize the observation of ultralow κ_L in both $PbSnS_3$ and $PbSnS_2$. The low dimensionality of both structures (1D for $PbSnS_3$ and 2D for $PbSnS_2$), characterized by weak Pb···S interchain interactions in $PbSnS_3$ and weak interlayer (Pb,Sn)-L···(Pb,Sn) interactions via the L lone pair of electrons of divalent cations in $PbSnS_2$, supports this statement. Similar conclusions have been also reported recently by Hua *et al*.[79] in their study of the anisotropic transport properties of $PbSnS_3$ single crystals. However, the authors considered $PbSnS_3$ has a "*non-layered structure*", *i.e*. a 3D structure, with high contrast of chemical bond strength ("*maldistribution"*) between the intra Sn-S bonds and inter Pb···S interactions. However, according to our structural description, $PbSnS_3$ must be described as a 1D structure whose $[Sn_2Pb_2S_6]$ chains are characterized by both strong intrachain Sn-S (2.56 to 2.63 Å) and Pb-S (2.78 to 2.94 Å) ionocovalent bonds, interconnected by weak interchain Pb···S interactions (3.08 to 3.42 Å, **Figure 1a**). $PbSnS_3$ is thus not a 3D compound but a 1D compound with strong bonds along the *b*-axis. This statement is well supported by the theoretical results of Hua *et al*. which show that the highest calculated κ_L is along the *b*-axis while the lowest κ_L is along the *a*- and *c*-axis. Hua *et al*. considered that this feature *« is not the common case in layered materials where the lowest κ is along the direction of breathing mode (cross plane)* ». However, the description of the 1D structure in our study with strong $[Sn_2Pb_2S_6]$ chains running along the *b*-axis fully justifies lowest κ_L values along the directions orthogonal to the *b*-axis. On the other hand, the presence of stereochemically active Sn^{2+} $5s^2$ lone-pairs electrons in $PbSnS_2$ amplifies the antibonding valence states and enhances the phonon anharmonicity, thereby inducing a lower κ_L in $PbSnS_2$ compared to $PbSnS_3$.

Conclusions

In conclusion, we have demonstrated that the origin of low lattice thermal conductivity (κ_L) in $PbSnS_3$ and $PbSnS_2$ sulphides is closely related to the combination of the low dimensionality of their structures with the stereochemical activity of their lone pair electrons cations. Although both metal sulphides exhibit low κ_L, the temperature dependence is significantly different due to the different dimensionality of their structures which is 1D for $PbSnS_3$ and 2D for $PbSnS_2$. Consequently, the interchain/interlayer interactions generated by the lone pair electrons of divalent cations are different in the two compounds, i.e. weak Pb···S interchain interactions in $PbSnS_3$ and weak interlayer (Pb,Sn)-L···(Pb,Sn) interactions via the L lone pairs in $PbSnS_2$. The low dimensionality of the crystal structures implying weak interchain and interlayer bonding and, as a consequence, lattice softening appears as the driven mechanism for phonon

scattering in these materials, which results in inherently low lattice thermal conductivity (κ_L) in both compounds. To unearth the various features of thermal conductivity in these compounds, we have performed in-depth experimental as well as theoretical analysis. The presence of soft lattice structure results in very soft acoustic phonon branches with frequency below 40 cm^{-1} in all directions in the Brillouin zone. These soft acoustics phonon branches are strongly scattered by the presence of numerous low-lying optical phonon modes which originate from the presence of stereochemically active lone pair of electrons and antibonding states below the fermi level (E_F). The presence of these low-lying optical phonon modes is further confirmed via low-temperature heat capacity data (C_p). These exciting phonon transport properties with very low κ_L and their unusual temperature dependency evidence the rich interplay between structural chemistry and thermal/vibrational properties which will be useful in diverse applications including optoelectronics and thermoelectrics.

Associated Content

Supporting Information (SI)

The Supporting Information is available free of charge on the ACS Publication website.

Experimental Section, Crystal structure, additional XRD data, Rietveld refinement of PXRD patterns, Mössbauer spectra, FESEM, electrical conductivity and Seebeck coefficient, optical absorption spectra, heat capacity data, eigenvector visualizations, electronic structure, interatomic force constants, thermal diffusivity, Rietveld refinement parameters, ^{119}Sn hyperfine parameters, sound velocity, parameters from Cp/T *vs.* T^2 fit, Callaway Model fitted parameter, experimental density, schematics of molecular orbital diagram.

Notes

The authors declare no competing financial interest.

Acknowledgments

The authors gratefully thank Christelle Bilot, Jerôme Lecourt and Thierry Schweitzer for technical support. P.A. and E.G thanks Normandy Region for financial support. K.P. acknowledges financial support from the Initiation Grant by Indian Institute of Technology Kanpur. The use of PARAM Sanganak under the National Supercomputing Mission, Government of India at the Indian Institute of Technology, Kanpur is gratefully acknowledged. X. S. acknowledges funding from the European Union's Horizon 2020 research and innovation

program under the Marie Sklodowska-Curie grant agreement No. 101034329, and the WINNING-Normandy program supported by the Normandy Region.

References

(1) Qian, X.; Zhou, J.; Chen, G. Phonon-engineered extreme thermal conductivity materials. *Nat. Mater.* **2021**, *20*, 1188-1202.

(2) Kim, H.; Park, G.; Park, S.; Kim, W. Strategies for Manipulating Phonon Transport in Solids. *ACS Nano* **2021**, *15*, 2182-2196.

(3) Ghosh, T.; Dutta, M.; Sarkar, D.; Biswas, K. Insights into Low Thermal Conductivity in Inorganic Materials for Thermoelectrics. *J. Am. Chem. Soc.* **2022**, *144*, 10099-10118.

(4) He, J.; Xia, Y.; Lin, W.; Pal, K.; Zhu, Y.; Kanatzidis, M. G.; Wolverton, C. Accelerated Discovery and Design of Ultralow Lattice Thermal Conductivity Materials Using Chemical Bonding Principles. *Adv. Funct. Mater.* **2022**, *32*, 2108532.

(5) Gibson, Q. D.; Zhao, T.; Daniels, L. M.; Walker, H. C.; Daou, R.; Hébert, S.; Zanella, M.; Dyer, M. S.; Claridge, J. B.; Slater, B.; et al. Low thermal conductivity in a modular inorganic material with bonding anisotropy and mismatch. *Science* **2021**, *373*, 1017-1022.

(6) Dames, C. Ultrahigh thermal conductivity confirmed in boron arsenide. *Science* **2018**, *361*, 549-550.

(7) Tian, F.; Song, B.; Chen, X.; Ravichandran, N. K.; Lv, Y.; Chen, K.; Sullivan, S.; Kim, J.; Zhou, Y.; Liu, T.-H.; et al. Unusual high thermal conductivity in boron arsenide bulk crystals. *Science* **2018**, *361*, 582-585.

(8) Padture, N. P.; Gell, M.; Jordan, E. H. Thermal Barrier Coatings for Gas-Turbine Engine Applications. *Science* **2002**, *296*, 280-284.

(9) Yang, J.; Wen, X.; Xia, H.; Sheng, R.; Ma, Q.; Kim, J.; Tapping, P.; Harada, T.; Kee, T. W.; Huang, F.; et al. Acoustic-optical phonon up-conversion and hot-phonon bottleneck in lead-halide perovskites. *Nat. Commun.* **2017**, *8*, 14120.

(10) Yan, Q.; Kanatzidis, M. G. High-performance thermoelectrics and challenges for practical devices. *Nat. Mater.* **2022**, *21*, 503-513.

(11) Shi, X.-L.; Zou, J.; Chen, Z.-G. Advanced Thermoelectric Design: From Materials and Structures to Devices. *Chem. Rev.* **2020**, *120*, 7399-7515.

(12) Biswas, K.; He, J.; Blum, I. D.; Wu, C.-I.; Hogan, T. P.; Seidman, D. N.; Dravid, V. P.; Kanatzidis, M. G. High-performance bulk thermoelectrics with all-scale hierarchical architectures. *Nature* **2012**, *489*, 414-418.

(13) Christensen, M.; Abrahamsen, A. B.; Christensen, N. B.; Juranyi, F.; Andersen, N. H.; Lefmann, K.; Andreasson, J.; Bahl, C. R. H.; Iversen, B. B. Avoided crossing of rattler modes in thermoelectric materials. *Nat. Mater.* **2008**, *7*, 811-815.

(14) Jiang, B.; Yu, Y.; Cui, J.; Liu, X.; Xie, L.; Liao, J.; Zhang, Q.; Huang, Y.; Ning, S.; Jia, B.; et al. High-entropy-stabilized chalcogenides with high thermoelectric performance. *Science* **2021**, *371*, 830-834.

(15) Chang, C.; Zhao, L.-D. Anharmoncity and low thermal conductivity in thermoelectrics. *Mater. Today Phys.* **2018**, *4*, 50-57.

(16) Shi, X.; Yang, J.; Salvador, J. R.; Chi, M.; Cho, J. Y.; Wang, H.; Bai, S.; Yang, J.; Zhang, W.; Chen, L. Multiple-Filled Skutterudites: High Thermoelectric Figure of Merit through Separately Optimizing Electrical and Thermal Transports. *J. Am. Chem. Soc.* **2011**, *133*, 7837-7846.

(17) Takabatake, T.; Suekuni, K.; Nakayama, T.; Kaneshita, E. Phonon-glass electron-crystal thermoelectric clathrates: Experiments and theory. *Rev. Mod. Phys.* **2014**, *86*, 669-716.

(18) Slack, G. A. Nonmetallic crystals with high thermal conductivity. *J. Phys. Chem. Solids* **1973**, *34*, 321-335.

(19) He, W.; Wang, D.; Wu, H.; Xiao, Y.; Zhang, Y.; He, D.; Feng, Y.; Hao, Y.-J.; Dong, J.-F.; Chetty, R.; et al. High thermoelectric performance in low-cost $SnS_{0.91}Se_{0.09}$ crystals. *Science* **2019**, *365*, 1418-1424.

(20) Lemoine, P.; Guélou, G.; Raveau, B.; Guilmeau, E. Crystal Structure Classification of Copper-Based Sulfides as a Tool for the Design of Inorganic Functional Materials. *Angew. Chem., Int. Ed.* **2022**, *61*, e202108686.

(21) Bourgès, C.; Bouyrie, Y.; Supka, A. R.; Al Rahal Al Orabi, R.; Lemoine, P.; Lebedev, O. I.; Ohta, M.; Suekuni, K.; Nassif, V.; Hardy, V.; et al. High-Performance Thermoelectric Bulk Colusite by Process Controlled Structural Disordering. *J. Am. Chem. Soc.* **2018**, *140*, 2186-2195.

(22) Suekuni, K.; Shimizu, Y.; Nishibori, E.; Kasai, H.; Saito, H.; Yoshimoto, D.; Hashikuni, K.; Bouyrie, Y.; Chetty, R.; Ohta, M.; et al. Atomic-scale phonon scatterers in thermoelectric colusites with a tetrahedral framework structure. *J. Mater. Chem. A* **2019**, *7*, 228-235, 10.1039/C8TA08248K.

(23) Guélou, G.; Lemoine, P.; Raveau, B.; Guilmeau, E. Recent developments in high-performance thermoelectric sulphides: an overview of the promising synthetic colusites. *J. Mater. Chem. C* **2021**, *9*, 773-795, 10.1039/D0TC05086E.

(24) He, Y.; Day, T.; Zhang, T.; Liu, H.; Shi, X.; Chen, L.; Snyder, G. J. High Thermoelectric Performance in Non-Toxic Earth-Abundant Copper Sulfide. *Adv. Mater.* **2014**, *26*, 3974-3978.

(25) Liu, H.; Shi, X.; Xu, F.; Zhang, L.; Zhang, W.; Chen, L.; Li, Q.; Uher, C.; Day, T.; Snyder, G. J. Copper ion liquid-like thermoelectrics. *Nat. Mater.* **2012**, *11*, 422-425.

(26) Rathore, E.; Juneja, R.; Culver, S. P.; Minafra, N.; Singh, A. K.; Zeier, W. G.; Biswas, K. Origin of Ultralow Thermal Conductivity in n-Type Cubic Bulk AgBiS2: Soft Ag Vibrations and Local Structural Distortion Induced by the Bi 6s2 Lone Pair. *Chem. Mater.* **2019**, *31*, 2106-2113.

(27) Feng, Z.; Jia, T.; Zhang, J.; Wang, Y.; Zhang, Y. Dual effects of lone-pair electrons and rattling atoms in $CuBiS_2$ on its ultralow thermal conductivity. *Phys. Rev. B* **2017**, *96*, 235205.

(28) Carnevali, V.; Mukherjee, S.; Voneshen, D. J.; Maji, K.; Guilmeau, E.; Powell, A. V.; Vaqueiro, P.; Fornari, M. Lone Pair Rotation and Bond Heterogeneity Leading to Ultralow Thermal Conductivity in Aikinite. *J. Am. Chem. Soc.* **2023**, *145*, 9313-9325.

(29) Dong, Y.; Khabibullin, A. R.; Wei, K.; Salvador, J. R.; Nolas, G. S.; Woods, L. M. Bournonite $PbCuSbS_3$: Stereochemically Active Lone-Pair Electrons that Induce Low Thermal Conductivity. *ChemPhysChem* **2015**, *16*, 3264-3270.

(30) Maji, K.; Lemoine, P.; Renaud, A.; Zhang, B.; Zhou, X.; Carnevali, V.; Candolfi, C.; Raveau, B.; Al Rahal Al Orabi, R.; Fornari, M.; et al. A Tunable Structural Family with Ultralow Thermal Conductivity: Copper-Deficient $Cu_{1-x}\square_xPb_{1-x}Bi_{1+x}S_3$. *J. Am. Chem. Soc.* **2022**, *144*, 1846-1860.

(31) Lu, X.; Morelli, D. T.; Xia, Y.; Zhou, F.; Ozolins, V.; Chi, H.; Zhou, X.; Uher, C. High Performance Thermoelectricity in Earth-Abundant Compounds Based on Natural Mineral Tetrahedrites. *Adv. Energy Mater.* **2013**, *3*, 342-348.

(32) Suekuni, K.; Tsuruta, K.; Kunii, M.; Nishiate, H.; Nishibori, E.; Maki, S.; Ohta, M.; Yamamoto, A.; Koyano, M. High-performance thermoelectric mineral $Cu_{12-x}Ni_xSb4S_{13}$ tetrahedrite. *J. Appl. Phys.* **2013**, *113*, 043712.

(33) Tan, G.; Hao, S.; Zhao, J.; Wolverton, C.; Kanatzidis, M. G. High Thermoelectric Performance in Electron-Doped $AgBi_3S_5$ with Ultralow Thermal Conductivity. *J. Am. Chem. Soc.* **2017**, *139*, 6467-6473.

(34) Bhui, A.; Dutta, M.; Mukherjee, M.; Rana, K. S.; Singh, A. K.; Soni, A.; Biswas, K. Ultralow Thermal Conductivity in Earth-Abundant $Cu_{1.6}Bi_{4.8}S_8$: Anharmonic Rattling of Interstitial Cu. *Chem. Mater.* **2021**, *33*, 2993-3001.

(35) Xia, Y.; Ozoliņš, V.; Wolverton, C. Microscopic Mechanisms of Glasslike Lattice Thermal Transport in Cubic $Cu_{12}Sb_4S_{13}$ Tetrahedrites. *Phys. Rev. Let.* **2020**, *125*, 085901.

(36) Lai, W.; Wang, Y.; Morelli, D. T.; Lu, X. From Bonding Asymmetry to Anharmonic Rattling in $Cu_{12}Sb_4S_{13}$ Tetrahedrites: When Lone-Pair Electrons Are Not So Lonely. *Adv. Funct. Mater.* **2015**, *25*, 3648-3657.

(37) Tan, Q.; Zhao, L.-D.; Li, J.-F.; Wu, C.-F.; Wei, T.-R.; Xing, Z.-B.; Kanatzidis, M. G. Thermoelectrics with earth abundant elements: low thermal conductivity and high thermopower in doped SnS. *J. Mater. Chem. A* **2014**, *2*, 17302-17306.

(38) Zhou, B.; Li, S.; Li, W.; Li, J.; Zhang, X.; Lin, S.; Chen, Z.; Pei, Y. Thermoelectric Properties of SnS with Na-Doping. *ACS Appl. Mater. Interfaces* **2017**, *9*, 34033-34041.

(39) Zhan, S.; Hong, T.; Qin, B.; Zhu, Y.; Feng, X.; Su, L.; Shi, H.; Liang, H.; Zhang, Q.; Gao, X.; et al. Realizing high-ranged thermoelectric performance in $PbSnS_2$ crystals. *Nat. Commun.* **2022**, *13*, 5937.

(40) Paar, W. H.; Miletich, R.; Topa, D.; Criddle, A. J.; Brodtkorb, M. K. D.; Amthauer, G.; Tippelt, G. Suredaite, $PbSnS_3$, a new mineral species, from the Pirquitas Ag-Sn deposit, NW-Argentina: mineralogy and crystal structure. *Am. Mineral.* **2000**, *85*, 1066-1075.

(41) Jumas, J. C.; Ribes, M.; Philippot, E.; Maurin, M. Sur filesysteme (SnS_2)(PbS), Structure cristalline de $PbSnS_3$. *C. R. Seances Acad.* **1972**, *275*, 269-271.

(42) Yamaoka, S.; Okai, B. Preparations of $BaSnS_3$, $SrSnS_3$ and $PbSnS_3$ at high pressure. *Mater. Res. Bull.* **1970**, *5*, 789-794.

(43) Prior, G. T. On Teallite, a new sulphostannite of lead from Bolivia ; and its relations to Franckeite and Cylindrite. *Mineral. Mag. J. Mineral. Soc.* **1904**, *14*, 21-27.

(44) Leute, V.; Behr, A.; Hünting, C.; Schmidtke, H. M. Phase diagram and diffusion properties of the quasibinary system (Sn, Pb)S. *Solid State Ion.* **1994**, *68*, 287-294.

(45) Lebedev, A.; Sluchinskaya, I.; Munro, I. EXAFS study of PbS-SnS solid solution. *J. Synchrotron Rad.* **2001**, *8*, 800-802.

(46) Hayashi, K.; Kitakaze, A.; Sugaki, A. A re-examination of herzenbergite–teallite solid solution at temperatures between 300 and 700°C. *Mineral. Mag.* **2001**, *65*, 645-651.

(47) Krebs, H.; Langner, D. Über Struktur und Eigenschaften der Halbmetalle. XVI. Mischkristallsysteme zwischen halbleitenden Chalkogeniden der vierten Hauptgruppe. II. *Z. Anorg. Allg. Chem.* **1964**, *334*, 37-49.

(48) Wiedemeier, H.; Georg, H.; Schnering, G. v. Refinement of the structures of GeS, GeSe, SnS and SnSe. *Z. fur Krist. - Cryst. Mater.* **1978**, *148*, 295-304.

(49) Shannon, R. D.; Prewitt, C. T. Revised values of effective ionic radii. *Acta Cryst.* **1970**, *26*, 1046-1048.

(50) Soriano, R. B.; Malliakas, C. D.; Wu, J.; Kanatzidis, M. G. Cubic Form of $Pb_{2-x}Sn_xS_2$ Stabilized through Size Reduction to the Nanoscale. *J. Am. Chem. Soc.* **2012**, *134*, 3228-3233.

(51) Ioannidou, C.; Lioutas, C. B.; Frangis, N.; Girard, S. N.; Kanatzidis, M. G. Analysis and Implications of Structural Complexity in Low Lattice Thermal Conductivity High Thermoelectric Performance PbTe–$PbSnS_2$ Composites. *Chem. Mater.* **2016**, *28*, 3771-3777.

(52) Gemmi, M.; Mugnaioli, E.; Gorelik, T. E.; Kolb, U.; Palatinus, L.; Boullay, P.; Hovmöller, S.; Abrahams, J. P. 3D Electron Diffraction: The Nanocrystallography Revolution. *ACS Cent. Sci.* **2019**, *5*, 1315-1329.

(53) Lippens, P. E. Interpretation of the ^{119}Sn Mossbauer isomer shifts in complex tin chalcogenides. *Phys. Rev. B* **1999**, *60*, 4576-4586.

(54) Greatrex, R.; Greenwood, N. N.; Ribes, M. Mössbauer spectra of ternary tin(IV) sulphides in the systems Na2S–SnS2, BaS–SnS2, and PbS–SnS2. *J. Chem. Soc., Dalton Trans.,* **1976**, 500-504, 10.1039/DT9760000500.

(55) Bourgès, C.; Lemoine, P.; Lebedev, O. I.; Daou, R.; Hardy, V.; Malaman, B.; Guilmeau, E. Low thermal conductivity in ternary $Cu_4Sn_7S_{16}$ compound. *Acta Mater.* **2015**, *97*, 180-190.

(56) Stephens, P. W. Phenomenological model of anisotropic peak broadening in powder diffraction. *J. Appl. Cryst.* **1999**, *32*, 281-289.

(57) Marinković, V.; Amelinckx, S. Anti-Phase Domains and Dislocation Ribbons in Tealite ($PbSnS_2$). *Phys. Stat. Sol. (b)* **1964**, *6*, 823-837.

(58) Brazda, P.; Klementova, M.; Krysiak, Y.; Palatinus, L. Accurate lattice parameters from 3D electron diffraction data. I. Optical distortions. *IUCrJ* **2022**, *9*, 735-755.

(59) de Kergommeaux, A.; Faure-Vincent, J.; Pron, A.; de Bettignies, R.; Malaman, B.; Reiss, P. Surface Oxidation of Tin Chalcogenide Nanocrystals Revealed by ^{119}Sn–Mössbauer Spectroscopy. *J. Am. Chem. Soc.* **2012**, *134*, 11659-11666.

(60) Lippens, P. E.; Olivier-Fourcade, J.; Jumas, J. C. Interpretation of the 119Sn Mössbauer parameters. *Hyperfine Interactions* **2000**, *126*, 137-141.

(61) Wagner, G.; Kaden, R.; Lazenka, V.; Bente, K. Microstructure of $Sn_{1-x}Pb_xS$ grown by hot-wall technique. *Phys. Status Solidi A* **2011**, *208*, 2150-2158.

(62) Le Dréau, L.; Prestipino, C.; Hernandez, O.; Schefer, J.; Vaughan, G.; Paofai, S.; Perez-Mato, J. M.; Hosoya, S.; Paulus, W. Structural Modulation and Phase Transitions in $La_2CoO_{4.14}$ Investigated by Synchrotron X-ray and Neutron Single-Crystal Diffraction. *Inorg. Chem.* **2012**, *51*, 9789-9798.

(63) Le Tonquesse, S.; Verastegui, Z.; Huynh, H.; Dorcet, V.; Guo, Q.; Demange, V.; Prestipino, C.; Berthebaud, D.; Mori, T.; Pasturel, M. Magnesioreduction Synthesis of Co-Doped β-$FeSi_2$: Mechanism, Microstructure, and Improved Thermoelectric Properties. *ACS Appl. Energy Mat.* **2019**, *2*, 8525-8534.

(64) Chattopadhyay, T.; Pannetier, J.; Von Schnering, H. G. Neutron diffraction study of the structural phase transition in SnS and SnSe. *J. Phys. Chem. Solids* **1986**, *47*, 879-885.

(65) Sun, B.; Niu, S.; Hermann, R. P.; Moon, J.; Shulumba, N.; Page, K.; Zhao, B.; Thind, A. S.; Mahalingam, K.; Milam-Guerrero, J.; et al. High frequency atomic tunneling yields ultralow and glass-like thermal conductivity in chalcogenide single crystals. *Nat. Commun.* **2020**, *11*, 6039.

(66) Chiritescu, C.; Cahill, D. G.; Nguyen, N.; Johnson, D.; Bodapati, A.; Keblinski, P.; Zschack, P. Ultralow Thermal Conductivity in Disordered, Layered WSe_2 Crystals. *Science* **2007**, *315*, 351-353.

(67) Acharyya, P.; Ghosh, T.; Pal, K.; Rana, K. S.; Dutta, M.; Swain, D.; Etter, M.; Soni, A.; Waghmare, U. V.; Biswas, K. Glassy thermal conductivity in $Cs_3Bi_2I_6Cl_3$ single crystal. *Nat. Commun.* **2022**, *13*, 5053.

(68) Dimitrov, I. K.; Manley, M. E.; Shapiro, S. M.; Yang, J.; Zhang, W.; Chen, L. D.; Jie, Q.; Ehlers, G.; Podlesnyak, A.; Camacho, J.; et al. Einstein modes in the phonon density of states of the single-filled skutterudite $Yb_{0.2}Co_4Sb_{12}$. *Phys. Rev. B* **2010**, *82*, 174301.

(69) Su, X.; Zhao, N.; Hao, S.; Stoumpos, C. C.; Liu, M.; Chen, H.; Xie, H.; Zhang, Q.; Wolverton, C.; Tang, X.; et al. High Thermoelectric Performance in the Wide Band-Gap $AgGa_{1-x}Te_2$ Compounds: Directional Negative Thermal Expansion and Intrinsically Low Thermal Conductivity. *Adv. Funct. Mater.* **2019**, *29*, 1806534.

(70) Xiao, Y.; Chang, C.; Pei, Y.; Wu, D.; Peng, K.; Zhou, X.; Gong, S.; He, J.; Zhang, Y.; Zeng, Z.; et al. Origin of low thermal conductivity in SnSe. *Phys. Rev. B* **2016**, *94*, 125203.

(71) Callaway, J. Model for Lattice Thermal Conductivity at Low Temperatures. *Phys. Rev.* **1959**, *113*, 1046-1051.

(72) Zhao, L.-D.; Lo, S.-H.; Zhang, Y.; Sun, H.; Tan, G.; Uher, C.; Wolverton, C.; Dravid, V. P.; Kanatzidis, M. G. Ultralow thermal conductivity and high thermoelectric figure of merit in SnSe crystals. *Nature* **2014**, *508*, 373-377.

(73) Morelli, D. T.; Jovovic, V.; Heremans, J. P. Intrinsically Minimal Thermal Conductivity in Cubic I-V−VI2 Semiconductors. *Phys. Rev. Let.* **2008**, *101*, 035901.

(74) Dronskowski, R.; Bloechl, P. E. Crystal orbital Hamilton populations (COHP): energy-resolved visualization of chemical bonding in solids based on density-functional calculations. *J. Phys. Chem.* **1993**, *97*, 8617-8624.

(75) Yuan, J.; Chen, Y.; Liao, B. Lattice Dynamics and Thermal Transport in Semiconductors with Anti-Bonding Valence Bands. *J. Am. Chem. Soc.* **2023**, *145*, 18506-18515.

(76) Jana, M. K.; Biswas, K. Crystalline Solids with Intrinsically Low Lattice Thermal Conductivity for Thermoelectric Energy Conversion. *ACS Energy Lett.* **2018**, *3*, 1315-1324.

(77) Pal, K.; Xia, Y.; Shen, J.; He, J.; Luo, Y.; Kanatzidis, M. G.; Wolverton, C. Accelerated discovery of a large family of quaternary chalcogenides with very low lattice thermal conductivity. *NPJ Comput. Mater.* **2021**, *7*, 82.

(78) Pal, K.; Xia, Y.; Wolverton, C. Microscopic mechanism of unusual lattice thermal transport in $TlInTe_2$. *NPJ Comput. Mater.* **2021**, *7*, 5.

(79) Hua, Y.; Bai, W.; Dai, S.; He, R.; Nan, P.; Sun, L.; Yang, J.; Sun, B.; Ge, B.; Xiao, C.; et al. Maldistribution of Chemical Bond Strength Inducing Exceptional Anisotropy of Thermal Conductivity in Non-Layered Materials. *Angew. Chem., Int. Ed.* **2023**, *62*, e202303081.

Table of Content